POLITECNICO DI TORINO
Repository ISTITUZIONALE

Exploring Optimal Dark Current Design in HgCdTe Infrared Barrier Detectors: A TCAD and Semianalytic Investigation

Original
Exploring Optimal Dark Current Design in HgCdTe Infrared Barrier Detectors: A TCAD and Semianalytic Investigation / Vallone, Marco; Alasio, Matteo; Tibaldi, Alberto; Bertazzi, Francesco; Hanna, Stefan; Wegmann, Anne; Eich, Detlef; Figgemeier, Heinrich; Ghione, Giovanni; Goano, Michele. - In: IEEE PHOTONICS JOURNAL. - ISSN 1943-0655. - ELETTRONICO. - 16:1(2024), pp. 1-8. [10.1109/jphot.2023.3345544]

Availability:
This version is available at: 11583/2986385 since: 2024-03-18T13:55:00Z

Publisher:
IEEE

Published
DOI:10.1109/jphot.2023.3345544

Terms of use:

This article is made available under terms and conditions as specified in the corresponding bibliographic description in the repository

Publisher copyright

(Article begins on next page)

27 April 2024

Exploring Optimal Dark Current Design in HgCdTe Infrared Barrier Detectors: A TCAD and Semianalytic Investigation

Marco Vallone, Matteo G. C. Alasio, *Member, IEEE*, Alberto Tibaldi, *Member, IEEE*, Francesco Bertazzi, Stefan Hanna, Anne Wegmann, Detlef Eich, Heinrich Figgemeier, Giovanni Ghione, *Life Fellow, IEEE*, and Michele Goano, *Senior Member, IEEE*

***Abstract*—The dark current is a fundamental figure of merit to characterize the performance of high-sensitivity, low-noise mid- and far-infrared barrier photodetectors. In the context of HgCdTe barrier photodetectors, the trend is to use very low doping concentrations, in an attempt to minimize recombination processes. In the present work, through TCAD simulations, we delve deeper into the design of low-dark-current pBn detectors, showing the possible existence of an optimum doping. This occurrence is investigated and interpreted also by means of closed-form expressions for the lifetimes, emphasizing the role of the interplay between Auger and Shockley-Read-Hall generation processes.**

***Index Terms*—Modeling, photodetectors, semiconductor materials, theory and design.**

I. Introduction

THE dark current density J_{dark} is one of the most important figures of merit to characterize infrared (IR) photodetectors, as a lower dark current allows for improved detectivity, resulting from lower noise, and for the possibility of longer imaging integration times [1], [2]. The need to operate under cryogenic conditions in order to limit the dark current affects the size, operating cost, and reliability of detectors. This has motivated sustained efforts to develop high operating temperature (HOT) detectors, i.e., devices characterized by lower cooling requirements [3], [4], [5], [6]. On this pathway, in 2007 the infrared community proposed the "Rule 07" – a simple relationship representing an empirical fit on the best measured devices [7] – to be the fundamental metric for predicting the dark current in $Hg_{1-x}Cd_xTe$ IR detectors. In a few decades, the outstanding performance of this ternary alloy has enabled the development of four generations of large format IR detectors for imaging in space science, environmental monitoring, diagnostics, surveillance, security, defense, etc. [6], [8], [9], [10], [11], [12], [13], both for mid-wavelength (MWIR, $\lambda \in [3, 5]\,\mu\text{m}$) and long-wavelength (LWIR, $\lambda \in [8, 12]\,\mu\text{m}$) infrared bands. Rule 07 was originally intended for P-on-n photodiodes, but soon has been adopted as a reference by technologies other than the HgCdTe-based ones, such as type-II superlattice (T2SL) devices [14], [15], [16], quantum dot photodetectors [17], [18], [19], and devices based on two-dimensional materials [20].[1]

The dark current is largely determined by minority carrier lifetimes [8], [21], [22]. After a summary of the concepts of dark current, generation rates, and lifetimes, Section II describes barrier detectors [23], [24], [25], [26], [27], [28], one of the popular solutions for fabricating photodetectors with low dark current and HOT performance. Focusing on one of their possible variants, Section III presents technology computer-aided design (TCAD) simulations of the dark current for a MWIR photodetector. Visualizing the dark current as a function of the absorber doping density reveals the existence of an optimal doping. This result indicates that the race to achieve extremely low residual doping in the absorber, required, for example, in fully-depleted detectors [29], [30], [31], is probably not an appropriate technological target for barrier photodetectors. This is an important point of interest to manufacturers, since the optimal doping can lower the dark current to values comparable to Rule 07. It is to be remarked that a reduction in dark current leads to a reduction of the NEDT (Noise Equivalent Difference Temperature) and increases the specific detectivity D^*. The NEDT and D^* definitions include the quantum efficiency, the dark current and its effect on thermal noise, and are the figures of merit most adopted in the infrared community to quantify the photodetector performance [1].

Aiming to provide a strong, yet simple physical interpretation of such optimal doping, Section IV presents three popular

Manuscript received 9 November 2023; revised 15 December 2023; accepted 18 December 2023. Date of publication 21 December 2023; date of current version 29 January 2024. This work was supported in part by the European Union, through two initiatives of the Italian National Recovery and Resilience Plan (NRRP) of NextGenerationEU: the partnership on *Telecommunications of the Future* under Grant PE00000001 – Program "RESTART", and the National Centre for HPC, Big Data and Quantum Computing under Grant CN00000013 – CUP E13C22000990001. *(Corresponding author: Marco Vallone.)*

Marco Vallone, Matteo G. C. Alasio, and Giovanni Ghione are with the Dipartimento di Elettronica e Telecomunicazioni, Politecnico di Torino, 10129 Torino, Italy (e-mail: marco.vallone@polito.it).

Alberto Tibaldi, Francesco Bertazzi, and Michele Goano are with the Dipartimento di Elettronica e Telecomunicazioni, Politecnico di Torino, 10129 Torino, Italy, and also with IEIIT-CNR, 10129 Torino, Italy.

Stefan Hanna, Anne Wegmann, Detlef Eich, and Heinrich Figgemeier are with AIM Infrarot-Module GmbH, D-74072 Heilbronn, Germany.

Digital Object Identifier 10.1109/JPHOT.2023.3345544

[1]Regarding P-on-n, P^+nN^+ and similar strings, the conventional notation indicates with a capital P or N an acceptor- or donor-doped layer, respectively, with bandgap wider than the n- or p-doped absorber; a "plus" superscript indicates a high doping level.

© 2023 The Authors. This work is licensed under a Creative Commons Attribution 4.0 License. For more information, see https://creativecommons.org/licenses/by/4.0/

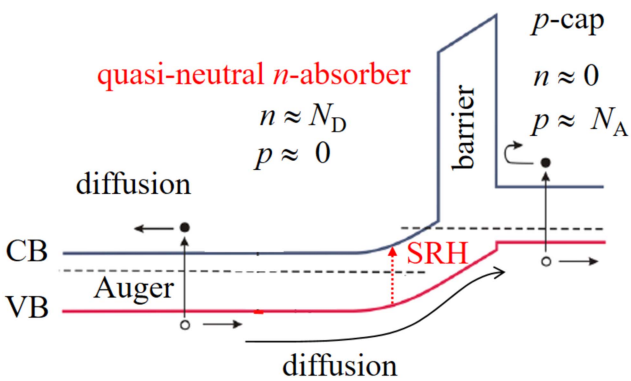

Fig. 1. Qualitative band diagram of a typical pBn barrier detector.

approximations to obtain n and p as function of T, N_D and N_A (the absolute temperature, the donors and acceptors concentrations, respectively). These expressions can be plugged into the generation rates and diffusion currents discussed in Section IV to achieve estimates of the dark current. Although not universal, these approximations allow, as discussed in Section V, to interpret the optimal doping as a result of the interplay between the Auger and Shockley-Read-Hall (SRH) carrier generation processes, and to provide design guidelines for barrier detectors. Finally, Section VI summarizes the main results.

II. Photodetectors, Lifetime and Dark Current: General Concepts

Conventional photodetectors are conceptually not so different from a pn-diode operated in reverse bias, for which most of the detector volume consists of two quite thick, p- and n-doped, quasi-neutral regions (QNRs), where the electric field appears negligible, whereas the space-charge region across the junction is normally much thinner (for precise definitions of QNRs and depleted regions see [32, Ch. 1-2]).

This work is focused on a different kind of photodetectors, i.e., on barrier detectors [24], [25], [33], [34]. Among the many variants of this class of devices, Fig. 1 represents a pBn detector: a thin layer of p-doped cap material, followed by a thin barrier of high bandgap material (represented by "B"), and finally the absorber, a layer of n-doped material whose thickness is in the order of the operating wavelength λ, therefore a few micrometers. Such detectors are also known as unipolar barrier detectors because, when a negative voltage is applied to the cap contact, the barrier blocks the electrons (in this case), but permits unimpeded flow of the absorber minority carriers (holes) towards the bias contact.

It is worth reminding that the dark current of a photodetector depends on the reverse bias voltage V_{bias}. In general, J_{dark} does not coincide with J_{diff}, and should be evaluated using a numerical simulator [32, Ch. 1.8]. In fact, the absorber can be partially depleted to an extent which depends on V_{bias}, and consequently it behaves only partially as a QNR. Furthermore, other contributions to J_{dark} come, e.g., from SRH generation in the barrier. Although J_{diff} and J_{dark} are different quantities, it will be interesting to compare their behavior against the absorber doping, when J_{dark} is simulated at a moderate reverse bias of the order of a few hundred millivolts.

The dark current receives contributions mainly from Auger, SRH, and radiative generation processes. Auger and SRH generation rates are given by [1], [24], [31], [35], [36], [37], [38], [39]

$$G_{\text{Auger}} = (n+p)\left(\frac{1}{2\tau^i_{\text{A1}}} + \frac{1}{2\tau^i_{\text{A7}}}\right) \tag{1}$$

$$G_{\text{SRH}} = \frac{n_i^2}{\tau_{\text{SRH}}(n+p+2n_i)} \tag{2}$$

respectively, where $\tau^i_{\text{A1,A7}}$ are the intrinsic A1, A7 Auger lifetimes [40], n_i is the intrinsic density, and τ_{SRH} is the SRH lifetime. G_{Auger} can also be written in the alternative form

$$G_{\text{Auger}} = \frac{n_i^2}{n\tau_{\text{A1}}} + \frac{n_i^2}{p\tau_{\text{A7}}} \tag{3}$$

which allows to single out the n- and p-dependent expressions for the Auger lifetimes,

$$\tau_{\text{A1}} = \frac{2\tau^i_{\text{A1}} n_i^2}{n(n+p)}, \quad \tau_{\text{A7}} = \frac{2\tau^i_{\text{A7}} n_i^2}{p(p+n)}. \tag{4}$$

The SRH lifetime τ_{SRH} is only related to the material defect density and carrier trapping cross sections [41], and thus it may be considered a technology-dependent parameter, not associated with any fundamental process.

We do not discuss here the contribution of radiative generation-recombination processes, since it depends on the detector geometry [42]. However, when appropriate, the concepts treated in this work can be extended including radiative recombinations without changing the general message conveyed by this study.

When a QNR is part of a photodetector, carriers generated by Auger and SRH processes diffuse towards the junction, where they eventually drift and, ultimately, are collected by the contacts. Hence, they are said to form a diffusion current J_{diff} originating from the QNR and concurring to build the dark current. In general, J_{dark} does not coincide with J_{diff}, and should be evaluated using a numerical simulator [32, Ch. 1.8].

It is worth reminding that the dark current of a photodetector depends on the reverse bias voltage V_{bias}. In fact, the absorber can be partially depleted to an extent which depends on V_{bias}, and consequently it behaves only partially as a QNR. Furthermore, other contributions to J_{dark} come, e.g., from SRH generation in the barrier. Although J_{diff} and J_{dark} are different quantities, it will be interesting to compare their behavior against the absorber doping, when J_{dark} is simulated at a moderate reverse bias of the order of a few hundred millivolts. J_{diff} can be written as

$$\begin{aligned} J_{\text{diff}} &= J_{\text{diff, Aug}} + J_{\text{diff, SRH}} \\ J_{\text{diff, Aug}} &= \text{q}tG_{\text{Auger}} \\ J_{\text{diff, SRH}} &= \text{q}tG_{\text{SRH}}, \end{aligned} \tag{5}$$

where q is the elementary charge and t the QNR thickness.

Equation (4) shows that the Auger lifetime is inversely proportional to the square of the majority carriers density, hence

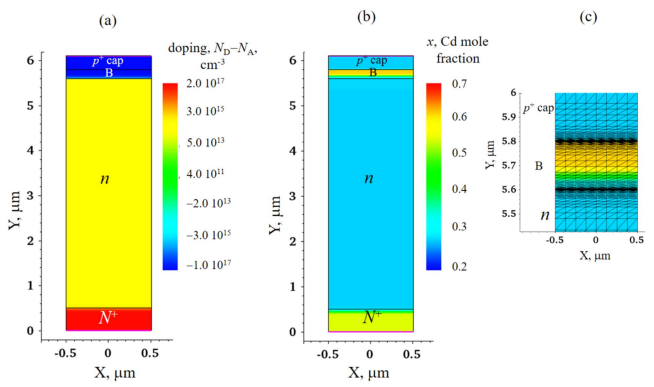

Fig. 2. Doping (a) and composition (b) profiles of the $p^+\mathrm{B}_p nN^+$ barrier photodetector simulated in Section III, with a detail (c) of the computational grid across the barrier layer.

$J_{\mathrm{diff,\,Aug}}$ increases proportionally to the latter, according to (1). Conversely, (2) shows that $J_{\mathrm{diff,\,SRH}}$ decreases as the carrier density increases, and these two opposite behaviors have the interesting consequences discussed in the next sections. It can be kept in mind, however, that contributions to dark current other than Auger, SRH and possibly radiative can be at play (tunneling, surface recombinations, etc.). Their relative importance depends on the details of the detector composition and geometry, on the material quality, and on the technology adopted for its fabrication. For a discussion see, e.g., [43, Ch. 5.3.2].

III. Dark Current in Barrier Detectors: Looking for Optimal Doping

We consider a simple one-dimensional model of a $p\mathrm{B}n$ photodetector (more precisely, a planar structure with a $p^+\mathrm{B}_p nN^+$doping scheme), whose doping and composition profiles are shown in Fig. 2. The layer stack is composed as follows: above a $0.5\ \mu$m-thick N^+ buffer layer ($\mathrm{Hg}_{0.45}\mathrm{Cd}_{0.55}\mathrm{Te}$, $N_\mathrm{D} = 2\times10^{17}$ cm $^{-3}$) are a $5\,\mu$m-thick absorber ($\mathrm{Hg}_{0.72}\mathrm{Cd}_{0.28}\mathrm{Te}$, donor-doped), followed by a $0.2\,\mu$m-thick barrier layer ($\mathrm{Hg}_{0.38}\mathrm{Cd}_{0.62}\mathrm{Te}$) and a $0.3\ \mu$m-thick cap layer ($\mathrm{Hg}_{0.7}\mathrm{Cd}_{0.3}\mathrm{Te}$), both acceptor-doped with $N_\mathrm{A} = 1\times10^{17}$ cm $^{-3}$. Doping the barrier with acceptors helps reducing the barrier in the valence band (important to efficiently collect the photogenerated minority carriers in the absorber), increasing in turn the barrier in the conduction band [33], [44]. The absorber doping varies in the interval $N_\mathrm{D} \in [10^{14}, 10^{17}]$ cm^{-3}, the operating temperature in $T \in [120, 200]$ K, and the SRH lifetime in $\tau_\mathrm{SRH} \in [10^{-1}, 10^{2}]\ \mu$s. The absorber cutoff wavelength is around $4.8\ \mu$m at 160 K, and it is the same material considered in [24, Fig. 24], where the authors investigated its properties with approximated expressions similar to (5). Between the layers, composition and doping varies smoothly to increase realism. Possible effects of annealing, that, in $n\mathrm{B}n$ detectors, could contribute to smoothing the barrier composition profile to a larger extent, undermining the detector performance [45], have not been considered, since the adopted $p^+\mathrm{B}_p nN^+$ profile is less affected by this detrimental effect [46]. Finally, since at the upper limit of the MWIR band the absorption length is about $3\,\mu$m at 160 K and about $5.7\ \mu$m at 200 K, a $5\ \mu$m-thick absorber should provide efficient absorption, without overly increasing the thermal carriers generation, which is proportional to the absorber volume.

This device is simulated with a numerical TCAD analysis tool, based on solving the quasi-static Poisson's equation self-consistently with the continuity equations of electrons and holes, the latter being closed with the drift-diffusion constitutive relations. A commercial simulation suite is employed, which is based on discretizing the differential operators with a stabilized finite-box method, and allows for great flexibility in the grid definition, enabling local refinements for critical regions (such as junctions between different materials and/or doping concentrations) [47]. Simulations take into account Fermi-Dirac statistics and incomplete dopant ionization, and employ temperature- and mole fraction-dependent material parameters according to [48] (Table I). The transport problem includes the SRH and Auger generation-recombination processes (modeled as in [41] and [49], respectively) and provides the steady-state solution at equilibrium and under reverse bias. A key difference vs. pn-photodetectors is that barrier detectors are quasi-unipolar and therefore do not require trap-assisted and band-to-band tunneling models [41], [50], [51], [52]. In addition, the electron barrier is thick enough to prevent any contribution from intraband tunneling.

Fig. 3(a) shows the band diagrams at $V_\mathrm{bias} = -0.2$ V, which indicates that only the electrons are blocked by the barrier, as required by a unipolar photodetector, while under illumination the photogenerated minority carriers – holes – are easily collected by the bias contact.

First, we simulated a set of *JV* characteristics for several values of N_D in the absorber, varying the bias voltage from the equilibrium to -0.2 V. We obtained a quite standard behavior, since the *JV* curves reach a sort of plateau, typical of diffusive, bias quasi-independent regime. However, importantly and in some way unexpectedly, the dark current density depends non-monotonically on N_D, as visible in Fig. 3(b).

Aiming at emphasizing this trend, Fig. 3(b) reports J_dark versus N_D at 160 K and fixed reverse voltage, for two values of τ_SRH. As a benchmark, we also report the expected dark current density according to Rule 07 for this temperature. The non-monotonic behavior clearly indicates the presence of an optimal absorber doping.

With this encouraging result, we managed to find a useful figure of merit to be plotted in the 2D domains described at the beginning of this section, aiming at characterizing the location of the minimum of J_dark. Since by changing the temperature and the SRH lifetime the current density varies of several orders of magnitude, the position of its minimum is most visible by plotting the logarithmic derivative of J_dark instead of J_dark itself, that is

$$D_\mathrm{log} = \left| \frac{1}{J_\mathrm{dark}} \frac{\mathrm{d}J_\mathrm{dark}}{\mathrm{d}N_\mathrm{D}} \right|_{V_\mathrm{bias}=-0.2\,\mathrm{V}}, \tag{6}$$

in the domain (T, N_D) for given τ_SRH and in the domain $(\tau_\mathrm{SRH}, N_\mathrm{D})$ for given T. These results are shown in Fig. 4, where the large dark blue bands in the two panels identify the vanishing of the J_dark derivative, i.e., the path followed by the

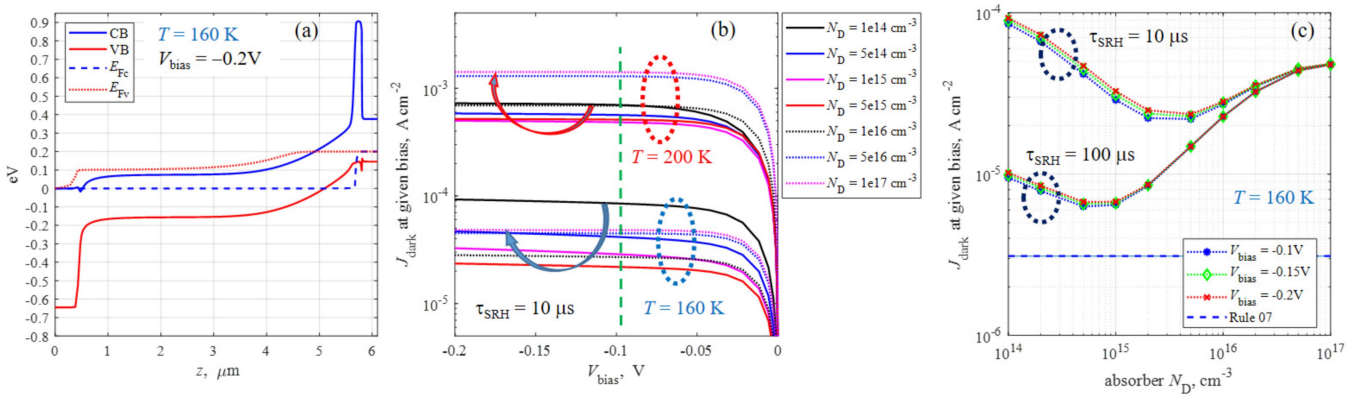

Fig. 3. (a) Band diagram $V_{\text{bias}} = -0.2$ V, (b) $J_{\text{dark}} - V$ characteristics for $\tau_{\text{SRH}} = 10\,\mu$s and two values of T (160 and 200 K). (c) J_{dark} at fixed reverse bias as function of the absorber doping, for $T = 160$ K and two values of τ_{SRH} (10 μs and 100 μs). A minimum for J_{dark} at fixed reverse bias is clearly visible.

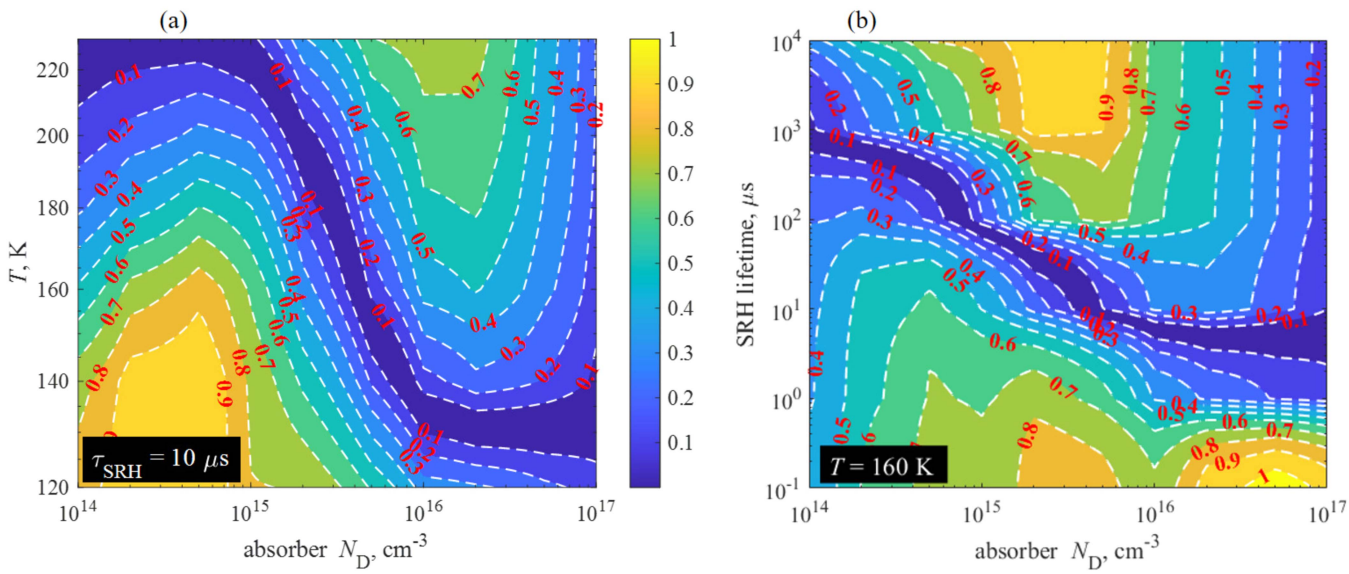

Fig. 4. 2D color map of $D_{\log}$, plotted (a) in the domain (T, N_{D}) for $\tau_{\text{SRH}} = 10\,\mu$s, and (b) in the domain $(\tau_{\text{SRH}}, N_{\text{D}})$ for $T = 160$ K. The dark blue region identifies the vanishing of the J_{dark} derivative, i.e., the path followed by the minimum of J_{dark} in the considered 2D simulation domain. In both panels $D_{\log}$ has been normalized to unity.

minimum of J_{dark} in the considered 2D simulation domains. It is important to observe that, for a given τ_{SRH} (in Fig. 4(a), 10 μs), the dark blue region extends almost vertically along a broad temperature interval. This means that the same doping value represents an optimal choice at least in the interval $160\,\text{K} < T < 200\,\text{K}$. Notice that the minimum of the dark current occurs for a reasonably broad range of absorber doping densities, compatible with the uncertainties introduced by technological processes. However, the same consideration does not apply to τ_{SRH}: Fig. 4(b) shows that different values of τ_{SRH} identify very different optimal doping values (the dark blue region is much less vertically oriented), hence a rough yet reliable estimate for τ_{SRH} should be obtained from characterizations of the material quality.

Color maps such as those in Fig. 4 provide a vivid representation of the 2D parameter space and some qualitative clues, such as the "optimal path" indicated by the dark blue bands. However, much more quantitative information is provided by 1D cuts, such as those shown in Fig. 3(c), which provide direct indications of the sensitivity of the dark current to the device parameters. For example, Fig. 3(c) not only indicates that, e.g., for $\tau_{\text{SRH}} = 10\,\mu$s, the optimal absorber doping is about 3×10^{15} cm^{-3}, but also that a doping reduction to 10^{14} cm^{-3} would make the dark current to increase by a factor of five, an effect that would thwart all the other efforts to obtaining high sensitivity photodetectors.

A further remark is in order, when discussing the available technology. The possibility to obtain minimal dark current for an intermediate doping, rather than for the lowest technologically-achievable doping as in the fully-depleted detectors, is an interesting result whenever the employed technology does not allow to reduce the SRH-related defect density [32], [41] to values so low to provide τ_{SRH} in the orders of milliseconds, as in the best fully-depleted detectors [31]. In more common cases, where τ_{SRH} is in the order of tens of microseconds as in Fig. 3(c), the

dark current reaches its minimum value when the absorber doping is between 10^{15} and 10^{16} cm^{-3}, an undoubtedly interesting value that can be achieved and managed with ease [53].

IV. Charge Carrier Density in QNR

When the absorber occupies the majority of the volume of the photodetector, it is often assumed in the literature [8], [21], [24] that the J_{diff} originated in the absorber, treated as QNR, is a reliable estimate of the total detector J_{dark}. Although this approach is not universally predictive, if the given constraint on the QNR thickness is verified, the general trend is sufficient to interpret the origin of the optimal doping. In this way, the simulation of the photodetector performance can be carried out by evaluating independently n and p, to be plugged in the generation rates described in Section II and then in the estimations of J_{diff}.

In the literature, three approximated formulations of increasing complexity can be found:

1) *simplest* approximation (SIM), where it is assumed

$$n = N_{\text{D}}, \quad p = 0 \qquad \text{in donor-doped regions}$$
$$n = 0, \quad p = N_{\text{A}} \qquad \text{in acceptor-doped regions}$$

in all generation-recombination rates and lifetimes expressions. It is an approximation adopted, e.g., in [8], [54], [55]

2) the *full dopants ionization* (FullDI), where n and p follow from the mass-action $np = n_i^2$ and the charge neutrality $n + N_{\text{A}} = p + N_{\text{D}}$ equations, which can be reformulated as

$$n = \frac{N_{\text{D}} - N_{\text{A}}}{2} + \left[\left(\frac{N_{\text{D}} - N_{\text{A}}}{2}\right)^2 + n_i^2\right]^{1/2}$$
$$p = \frac{N_{\text{A}} - N_{\text{D}}}{2} + \left[\left(\frac{N_{\text{A}} - N_{\text{D}}}{2}\right)^2 + n_i^2\right]^{1/2} \tag{7}$$

and which include a dependence on temperature through n_i

3) the *incomplete dopants ionization* (IncDI), where n and p are selfconsistently calculated from
   - the charge neutrality equation $n + N_{\text{A}}^- = p + N_{\text{D}}^+$
   - the Fermi levels $E_{F,n}$, $E_{F,p}$
   - the ionized dopant concentrations N_{A}^- and N_{D}^+

   whose expressions as function of N_{D}, N_{A} and T can be found in textbooks, (see, e.g., [32, Ch. 1.4]), assuming for dopants activation energies the values reported, e.g., in [1], [56] ($\approx$ 1 meV for donors and $\approx$ 20 meV for acceptors).

The accuracy of the estimates for n and p provided by SIM, FullDI, and IncDI varies and generally depends on temperature and doping. It must be noticed that the SIM approximation ignores the mass-action law. Consequently, in donor-doped semiconductors, it approximates p to zero instead of n_i^2/N_{D}. This can be a sort of simplification, and it can be acceptable only when $N_{\text{D}} \gg n_i$, which strongly depends on temperature (e.g., for MWIR when T is below $\approx$ 200 K).

Fig. 5 shows an example of calculation for a donor-doped $\text{Hg}_{1-x}\text{Cd}_x\text{Te}$ QNR with $x = 0.294$, for $T = 240$ K and $N_{\text{D}} \in [10^{12}, 10^{18}]$ cm^{-3}. It is apparent that:

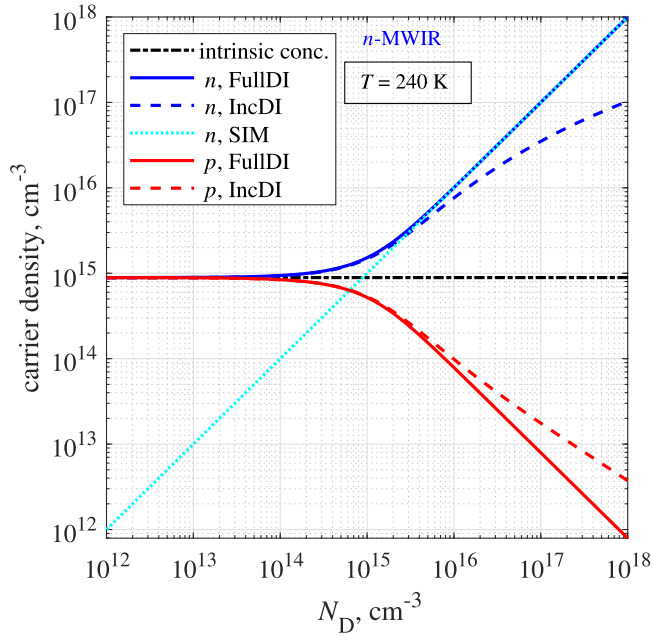

Fig. 5. Carrier density evaluated in the SIM, FullDI and IncDI approximations, for donor-doped $\text{Hg}_{1-x}\text{Cd}_x\text{Te}$ with $x = 0.294$, for $T = 240$ K. Notice that in the SIM approximation a donor-doped material has always $p = 0$.

- for $N_{\text{D}} >> n_i$, SIM and FullDI are quasi-equivalent: the calculated values of n are very similar, and FullDI estimates a value for p that is several orders of magnitude lower than n, hence negligible, at least with respect to it;
- for high N_{D}, e.g., $N_{\text{D}} \approx 10^{18}$ cm^{-3}, IncDI is the only acceptable approximation, as it provides an estimation for n which is one order of magnitude lower than that of the rougher FullDI and SIM, and the difference in some applications cannot be ignored;
- for $N_{\text{D}} << n_i$, the SIM approximation is not appropriate and provides wrong results both for n and p, since in a QNR n can never be lower than n_i. Instead, FullDI and IncDI are almost equivalent.

V. Literature Examples: Lifetimes and Diffusion Currents

Before investigating the origin of the optimal doping, it is important to validate the expressions in Section II by reproducing examples of calculation taken from the literature, comparing the results provided by the three approximations.

A. Example 1

As a first example, we have tried to reproduce the Auger lifetimes presented in [8, Fig. 3] calculating τ_{A1} and τ_{A7} at $T = 77$ K, respectively for n-doped and p-doped long-wavelength infrared (LWIR) $\text{Hg}_{1-x}\text{Cd}_x\text{Te}$ QNRs with $x = 0.23$, corresponding to a cutoff wavelength $\lambda_c = 9.5\,\mu$m at this temperature. Fig. 6(a) shows that the SIM and FullDI approximations are equivalent at this temperature (the curves overlap) and reproduce successfully the results from the reference, which

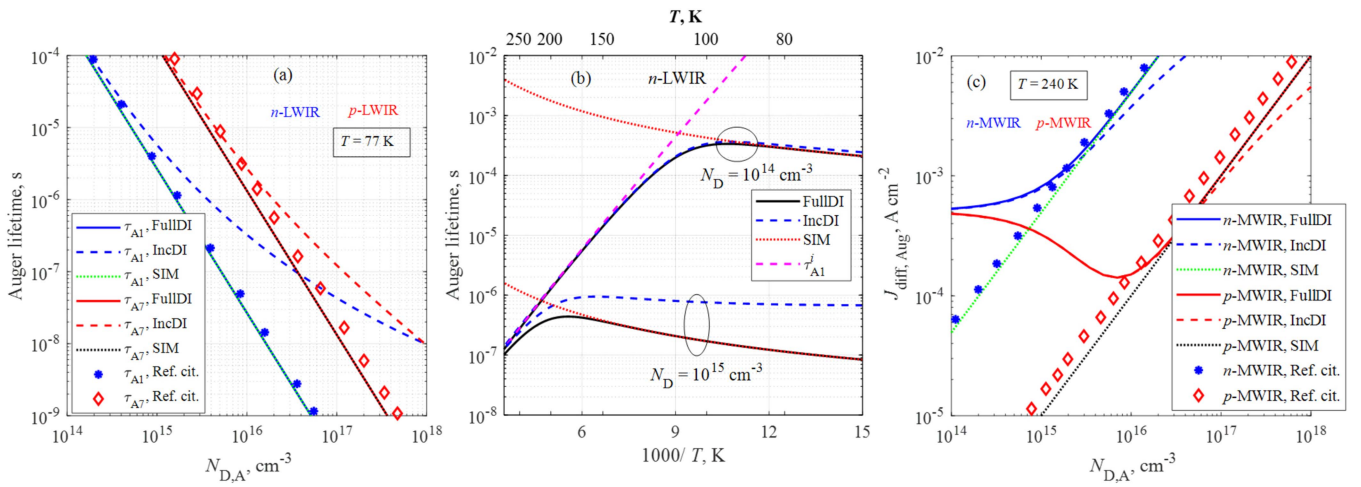

Fig. 6. (a) Auger lifetime vs. doping for n- and p-LWIR, at 77 K. Symbols are taken from [8, Fig. 3]. (b) Auger lifetime versus T for n-LWIR. (c) Auger diffusion current for n- and p-MWIR, at 240 K with parameters as in [8, Fig. 4]. Symbols are taken from [8, Fig. 4].

are also included in the same figure. At high doping densities, the effects of incomplete ionization of the dopants cannot be neglected, and indeed the IncDI curves diverge progressively: for $N_{\rm D} \approx 10^{18}$ cm^{-3} the deviation is of several orders of magnitude, and for this temperature the IncDI approximation would have been more appropriate. Fig. 6(b) shows that, conversely, as the temperature is increased toward room temperature, the effect of incomplete dopant ionization becomes increasingly less important and FullDI is a safe option. Instead, the SIM approach becomes completely inapplicable, as Fig. 5 had already indicated.

B. Example 2

As a second case study, we focus on the n-doped and p-doped mid-wave infrared (MWIR) photodetectors at $T = 240$ K from [8, Fig. 4], which are realized with $Hg_{1-x}Cd_xTe$, $x = 0.29$, having, at this temperature, cutoff wavelength $\lambda_c = 4.6\,\mu$m. The results of our calculations are reported in Fig. 6(c), which also includes the Auger lifetimes estimated from the Auger diffusion currents reported in [8] (solid dots). It is apparent that the SIM approximation accurately reproduces the data taken from the cited reference. As for the effects of incomplete dopant ionization, we see that at this relatively high temperature the IncDI deviates only minimally from the FullDI, and only in the direction of the highest dopant value, so there is no obvious need for its use.

A further remark about the SIM approximation: Fig. 6(b) shows that for $N_{\rm D} = 10^{14}$ cm^{-3} and $T > 200$ K the Auger lifetime $\tau_{\rm A1}$ calculated in the SIM approximation deviates by several orders of magnitude with respect to FullDI or IncDI, and the relative deviation increases rapidly with T. This because n_i rapidly increases with T according to [32, Ch. 1.4]

$$n_i \propto T^{3/2} e^{-\frac{E_{\rm g}}{2k_{\rm B}T}} \tag{8}$$

($E_{\rm g}$ is the material energy gap and $k_{\rm B}$ is the Boltzmann constant), and in the SIM approximation it is $\tau_{\rm A1} \propto (n_i/N_{\rm D})^2$, where $N_{\rm D}$ is fixed. The obtained lifetime is unphysical: for comparison, when T tends to room temperature, the Auger lifetimes obtained by the FullDI and IncDI approximations correctly tend to the intrinsic lifetime $\tau^i_{\rm A1}$. All this reflects on the calculation of the Auger diffusion current as shown in Fig. 6(c): the SIM approximation greatly underestimates $J_{\rm diff,\,Aug}$ because it overestimates $\tau_{\rm A1}$.

C. Example 3: The Origin of the Optimal Doping

The third example is engineered in order to shed light on the physical origin of the optimal doping. Specifically, we attempted to reproduce the total diffusion current according to (5) for a 3 μm-thick QNR with composition, temperature and doping values as in [24, Fig. 24], i.e., n-doped MWIR $Hg_{1-x}Cd_xTe$ with $x = 0.298$, and $T = 160$ K (at this temperature $\lambda_c = 4.8\,\mu$m). This is the same material employed as absorber layer in the drift-diffusion simulations described in Section III (see in particular Fig. 3(c)).

We consider three values of $\tau_{\rm SRH}$, representative of medium-quality material, i.e., 0.1, 1 and 10 μs, as in [24, Fig. 24]. Fig. 7 was obtained using the IncDI approximation, achieving a good agreement with the behavior in the reference. Corresponding results obtained with FullDI and SIM, not reproduced here for brevity, show very similar behavior, including the SIM approximation. The reason is the following: around the lowest considered dopant concentration, it is $\tau_{\rm SRH} \ll \tau_{\rm A1}$, i.e., the material is SRH-limited. Consequently, $J_{\rm diff}$ is dominated by $J_{\rm diff,\,SRH}$, which at this temperature depends on the adopted approximation to a very limited extent, in contrast to the scenario represented by Fig. 6(c).

It is important to remark that the optimal dopant concentration is approximately the same found when simulating the pBn photodetector with the TCAD numerical simulator. This is an important point, which was already remarked in [24], although without a detailed investigation. Fig. 7 clearly shows that the origin of the optimal doping is the interplay between the Auger and SRH generation, as anticipated when commenting (1)–(2).

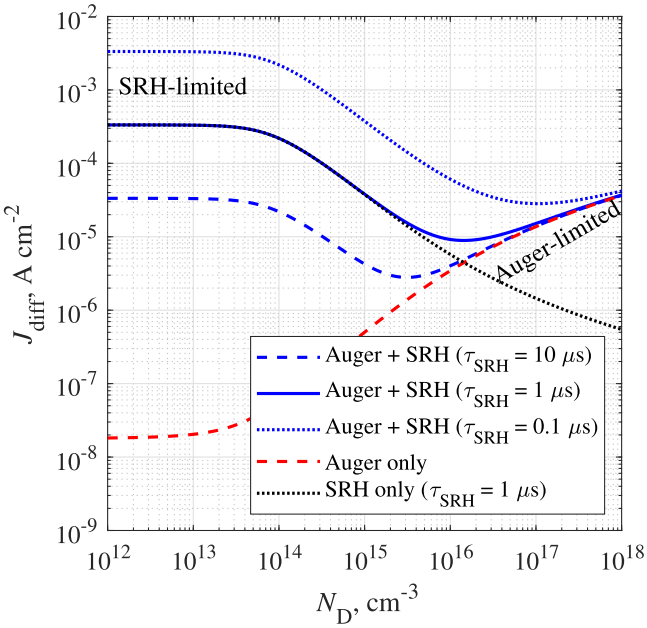

Fig. 7. Total diffusion current for n-MWIR at 160 K, for parameters as in [24, Fig. 24], IncDI approximation.

It is important to note that, although for $\tau_{SRH} = 10\,\mu$s the value of the optimal doping obtained by $J_{dark}(N_D)$ and $J_{diff}(N_D)$ is approximately the same, by contrast the minimum of J_{dark} is an order of magnitude larger than the corresponding minimum of J_{diff}. This confirms a partial depletion of the absorber – as also indicated by the band bending in Fig. 3(a) – which increases the contribution of SRH to dark current with respect of what calculated for an ideal QNR.

VI. Conclusion

This work presents an investigation about lifetime and dark current in HgCdTe IR photodetectors. In the first part we performed a set of numerical simulations with a semiclassical TCAD simulation suite for IR barrier detectors. The dark current presents an interesting non-monotonic behavior. In the parameter spaces (T, N_D) and (τ_{SRH}, N_D) a region of optimal doping can be seen at a glance, allowing to minimize the dark current for a given temperature and material quality (the latter represented by τ_{SRH}). Figs. 3 and 4 show that, at least for the considered material, the optimal doping lies in the interval $[10^{15}, 10^{16}]$ cm^{-3}; such values can be achieved by most manufacturers. Actually, considering that fully-depleted detectors require absorbers with ultra-low residual doping ($N_D \approx 10^{13}$ cm^{-3}), this finding strengthens the idea that barrier photodetectors can represent a useful alternative whenever the available technology cannot provide materials with such record characteristics.

An important topic not addressed in the present work is represented by the effects of doping, thickness and molar composition of the barrier and cap layers. These points deserve a dedicated investigation, since these parameters could affect both dark current and quantum efficiency. An extension of the present investigation towards the exploration of their possible effects on the optimal doping in $p\mathrm{B}_p n$ detectors is important and can be possibly the object of a future work. However, for a discussion concerning their effects on $n\mathrm{B}n$ detectors, see, e.g., [45].

In the second part of this work, aiming at achieving deeper insight into this property, we looked for a possible occurrence of an optimal doping targeting the minimum diffusion current generated in a QNR of doped HgCdTe. To this end, first we provided a critical review of three possible approximations employed in the literature to obtain the values of carrier density in HgCdTe based IR photodetectors. Each of them provides a different estimate of carrier lifetime and photodetector dark current, and the relative difference has been found to depend on temperature and doping concentration in a significant way. In some cases, such discrepancies cannot be neglected. Specifically, the SIM approximation tends to lose its validity when the doping is low and temperature is relatively high (see, e.g., Fig. 6(b) and (c) corresponding to 240 K), whereas it remains valid and in practice coincides with the FullDI when the temperature is particularly low (see, e.g., Fig. 6(a) corresponding to 77 K). Then, we calculated the diffusion current J_{diff} generated in a donor-doped quasi-neutral (or field-free) region as function of doping, having considered the same HgCdTe composition adopted for the TCAD simulations. J_{diff} has been found to have a non-monotonic behavior very similar to J_{dark}, and this behavior is shown to be related with the interplay between the Auger and SRH generation rates.

References

[1] A. Rogalski, *Infrared Detectors*, 2nd ed. Boca Raton, FL, USA: CRC Press, 2011.
[2] L. Zhu et al., "Low frequency noise–dark current correlations in HgCdTe infrared photodetectors," *Opt. Exp.*, vol. 28, no. 16, pp. 23660–23669, 2020.
[3] T. Ashley and C. T. Elliott, "Model for minority carrier lifetimes in doped HgCdTe," *Electron. Lett.*, vol. 21, no. 10, pp. 451–452, 1985.
[4] C. T. Elliott, "Non-equilibrium modes of operation of narrow-gap semiconductor devices," *Semicond. Sci. Technol.*, vol. 5, no. 35, 1990, Art. no. S30.
[5] P. Martyniuk and A. Rogalski, "HOT infrared photodetectors," *Opto-Electron. Rev.*, vol. 21, no. 2, pp. 239–257, 2013.
[6] A. Rogalski, P. Martyniuk, M. Kopytko, and W. Hu, "Trends in performance limits of the HOT infrared photodetectors," *Appl. Sci.*, vol. 11, no. 2, 2021, Art. no. 501.
[7] W. E. Tennant, D. Lee, M. Zandian, E. Piquette, and M. Carmody, "MBE HgCdTe technology: A very general solution to IR detection, described by "Rule 07," a very convenient heuristic," *J. Electron. Mater.*, vol. 37, no. 9, pp. 1406–1410, 2008.
[8] M. A. Kinch, F. Aqariden, D. Chandra, P.-K. Liao, H. F. Schaake, and H. D. Shih, "Minority carrier lifetime in p-HgCdTe," *J. Electron. Mater.*, vol. 34, no. 6, pp. 880–884, 2005.
[9] A. Rogalski, J. Antoszewski, and L. Faraone, "Third-generation infrared photodetector arrays," *J. Appl. Phys.*, vol. 105, no. 9, 2009, Art. no. 091101.
[10] M. A. Kinch, "HgCdTe: Recent trends in the ultimate IR semiconductor," *J. Electron. Mater.*, vol. 39, no. 7, pp. 1043–1052, 2010.
[11] P. Martyniuk, J. Antoszewski, M. Martyniuk, L. Faraone, and A. Rogalski, "New concepts in infrared photodetector designs," *Appl. Phys. Rev.*, vol. 1, 2014, Art. no. 041102.
[12] M. Reine, "Interview with Paul W. Kruse on the early history of HgCdTe, conducted on Oct. 22, 1980," *J. Electron. Mater.*, vol. 44, no. 9, pp. 2955–2968, 2015.
[13] O. Gravrand et al., "HgCdTe detectors for space and science imaging: General issues and latest achievements," *J. Electron. Mater.*, vol. 45, no. 9, pp. 4532–4541, 2016.
[14] A. Rogalski, P. Martyniuk, and M. Kopytko, "Type-II superlattice photodetectors versus HgCdTe photodiodes," *Prog. Quantum Electron.*, vol. 68, 2019, Art. no. 100228.

[15] F. Bertazzi, A. Tibaldi, M. Goano, J. A. G. Montoya, and E. Bellotti, "Nonequilibrium Green's function modeling of type-II superlattice detectors and its connection to semiclassical approaches," *Phys. Rev. Appl.*, vol. 14, no. 1, Jul. 2020, Art. no. 014083.

[16] A. Tibaldi, J. A. G. Montoya, M. Vallone, M. Goano, E. Bellotti, and F. Bertazzi, "Modeling infrared superlattice photodetectors: From nonequilibrium Green's functions to quantum-corrected drift diffusion," *Phys. Rev. Appl.*, vol. 16, no. 4, Oct. 2021, Art. no. 044024.

[17] W. Palosz et al., "HgTe quantum dots for near-, mid-, and long-wavelength IR devices," *J. Electron. Mater.*, vol. 46, no. 9, pp. 5411–5417, 2017.

[18] P. Guyot-Sionnest, M. M. Ackerman, and X. Tang, "Colloidal quantum dots for infrared detection beyond silicon," *J. Chem. Phys.*, vol. 151, no. 6, 2019, Art. no. 060901.

[19] H. Song, Y. Tischenko, D. Wasserman, and K. S. Jeong, "Quantum dot materials for mid-IR photodetection: Opinion," *Opt. Mater. Express*, vol. 13, no. 5, pp. 1328–1334, 2023.

[20] A. Rogalski, M. Kopytko, P. Martyniuk, and W. Hu, "Comparison of performance limits of HOT HgCdTe photodiodes with 2D material infrared photodetectors," *Opto-Electron. Rev.*, vol. 28, no. 2, pp. 82–92, 2020.

[21] M. Kopytko, J. Sobieski, W. Gawron, A. Kebłowski, and J. Piotrowski, "Minority carrier lifetime in HgCdTe(100) epilayers and their potential application to background radiation limited MWIR photodiodes," *Semicond. Sci. Technol.*, vol. 36, 2021, Art. no. 055003.

[22] K. Jóźwikowski, A. Jóźwikowska, and O. Markowska, "Calculation of minority carriers lifetime in HgCdTe structures by using the method based on mutual correlation between the concentration of electrical particles," *IEEE Trans. Electron Devices*, vol. 69, no. 4, pp. 1995–2001, Apr. 2022.

[23] S. Maimon and G. W. Wicks, "nBn detector, an infrared detector with reduced dark current and higher operating temperature," *Appl. Phys. Lett.*, vol. 89, no. 15, 2006, Art. no. 151109.

[24] P. Martyniuk, M. Kopytko, and A. Rogalski, "Barrier infrared detectors," *Opto-Electron. Rev.*, vol. 22, no. 2, pp. 127–146, 2014.

[25] O. Gravrand, F. Boulard, A. Ferron, P. Ballet, and W. Hassis, "A new nBn IR detection concept using HgCdTe material," *J. Electron. Mater.*, vol. 44, no. 9, pp. 3069–3075, 2015.

[26] I. D. Burlakov, N. A. Kulchitsky, A. V. Voitsekhovskii, S. N. Nesmelov, S. M. Dzyadukh, and D. I. Gorn, "Unipolar semiconductor barrier structures for infrared photodetector arrays (review)," *J. Commun. Technol. Electron.*, vol. 66, no. 9, pp. 1084–1091, 2021.

[27] Q. Shi, S.-K. Zhang, J.-L. Wang, and J.-H. Chu, "Progress on nBn infrared detectors," *J. Infrared Millimeter Waves*, vol. 41, no. 1, pp. 139–150, Feb. 2022.

[28] A. V. Voitsekhovskii et al., "Comprehensive experimental study of NBνN barrier structures based on n-HgCdTe MBE for detection in MWIR and LWIR spectra," *Physica Scripta*, vol. 98, no. 6, 2023, Art. no. 065907.

[29] J. Schuster, W. E. Tennant, E. Bellotti, and P. S. Wijewarnasuriya, "Analysis of the Auger recombination rate in $P^+N^-n^-N^-N$ HgCdTe detectors for HOT applications," *Proc. SPIE*, vol. 9819, 2016, Art. no. 98191F.

[30] D. Lee et al., "High-operating temperature HgCdTe: A vision for the near future," *J. Electron. Mater.*, vol. 45, no. 9, pp. 4587–4595, 2016.

[31] D. Lee et al., "Law 19: The ultimate photodiode performance metric," *Proc. SPIE*, vol. 11407, 2020, Art. no. 114070X.

[32] S. M. Sze and K. K. Ng, *Physics of Semiconductor Devices*, 3rd ed. Hoboken, NJ, USA: Wiley, 2007.

[33] M. Kopytko et al., "Status of HgCdTe barrier infrared detectors grown by MOCVD in Military University of Technology," *J. Electron. Mater.*, vol. 45, no. 9, pp. 4563–4573, 2016.

[34] I. I. Izhnin et al., "Unipolar superlattice structures based on MBE HgCdTe for infrared detection," *Appl. Nanosci.*, vol. 10, no. 12, pp. 4571–4576, 2020.

[35] F. Bertazzi, M. Goano, and E. Bellotti, "Calculation of Auger lifetime in HgCdTe," *J. Electron. Mater.*, vol. 40, no. 8, pp. 1663–1667, 2011.

[36] M. A. Kinch, *State-of-the-Art Infrared Detector Technology*. Bellingham, WA, USA: SPIE, 2014.

[37] P. Martyniuk and A. Rogalski, "MWIR barrier detectors versus HgCdTe photodiodes," *Infrared Phys. Technol.*, vol. 70, pp. 125–128, 2015.

[38] M. Kopytko and A. Rogalski, "New insights into the ultimate performance of HgCdTe photodiodes," *Sensors Actuators A: Phys.*, vol. 339, 2022, Art. no. 113511.

[39] M. Kopytko, "SRH suppression mechanism in a non-equilibrium MWIR HgCdTe photodiode," *Opto-Electron. Rev.*, vol. 31, 2023, Art. no. 144548.

[40] J. S. Blakemore, *Semiconductor Statistics*, vol. 3. New York, NY, USA: Pergamon, 1962.

[41] M. Vallone et al., "Numerical modeling of SRH and tunneling mechanisms in high-operating-temperature MWIR HgCdTe photodetectors," *J. Electron. Mater.*, vol. 44, no. 9, pp. 3056–3063, 2015.

[42] M. Kopytko, K. Jóźwikowski, P. Martyniuk, and A. Rogalski, "Photon recycling effect in small pixel p-i-n HgCdTe long wavelength-infrared photodiodes," *Infrared Phys. Technol.*, vol. 97, pp. 38–42, 2019.

[43] M. A. Kinch, *Fundamentals of Infrared Detector Materials*. Bellingham, WA, USA: SPIE, 2007.

[44] M. Kopytko et al., "MOCVD grown HgCdTe p^+BnN^+ barrier detector for MWIR HOT operation," in *Proc. SPIE Infrared Technol. Appl.*, 2015, Art. no. 945117.

[45] J. He et al., "Enhanced performance of HgCdTe long-wavelength infrared photodetectors with nBn design," *IEEE Trans. Electron Devices*, vol. 67, no. 5, pp. 2001–2007, May 2020.

[46] M. G. C. Alasio et al., "Modeling the effects of graded and abrupt mole fraction profiles in pBn and nBn HgCdTe barrier detectors," *Proc. SPIE*, vol. 12687, 2023, Art. no. 126870E.

[47] "Sentaurus device user guide. version N-2017.09," Synopsys, Inc., Mountain View, CA, USA, Sep. 2017.

[48] M. Vallone et al., "Simulation of small-pitch HgCdTe photodetectors," *J. Electron. Mater.*, vol. 46, no. 9, pp. 5458–5470, 2017.

[49] V. C. Lopes, A. J. Syllaios, and M. C. Chen, "Minority carrier lifetime in mercury cadmium telluride," *Semicond. Sci. Technol.*, vol. 8, 1993, Art. no. 824.

[50] M. Mandurrino et al., "Trap-assisted tunneling in InGaN/GaN LEDs: Experiments and physics-based simulation," in *Proc. 14th Int. Conf. Numer. Simul. Optoelectron. Devices*, 2014, pp. 13–14.

[51] M. Mandurrino et al., "Semiclassical simulation of trap-assisted tunneling in GaN-based light-emitting diodes," *J. Comput. Electron.*, vol. 14, no. 2, pp. 444–455, Jun. 2015.

[52] M. Mandurrino et al., "Physics-based modeling and experimental implications of trap-assisted tunneling in InGaN/GaN light-emitting diodes," *Physica Status Solidi A*, vol. 212, no. 5, pp. 947–953, 2015.

[53] H. Lutz, R. Breiter, D. Eich, H. Figgemeier, and S. Hanna, "Improved high performance MCT MWIR and LWIR modules," *Proc. SPIE*, vol. 11002, 2019, Art. no. 1100216.

[54] O. Gravrand, L. Mollard, C. Largeron, N. Baier, E. Deborniol, and P. Chorier, "Study of LWIR and VLWIR focal plane array developments: Comparison between p-on-n and different n-on-p technologies on LPE HgCdTe," *J. Electron. Mater.*, vol. 38, no. 8, pp. 1733–1740, 2009.

[55] V. Gopal, Q. Li, J. He, K. He, C. Lin, and W. Hu, "Current transport mechanisms in mercury cadmium telluride diode," *J. Appl. Phys.*, vol. 120, no. 8, 2016, Art. no. 084508.

[56] P. Capper and J. Garland, Eds., *Mercury Cadmium Telluride: Growth, Properties and Applications*. Chichester, U.K.: Wiley, 2011.

Open Access funding provided by 'Politecnico di Torino' within the CRUI CARE Agreement